Outdoor Wideband Channel Measurements and Modeling in the 3-18 GHz Band

Vinod Kristem, C. Umit Bas, *Student Member, IEEE,*
Rui Wang, *Student Member, IEEE*, and Andreas F. Molisch, *Fellow, IEEE,*

Abstract—Fifth generation cellular systems will operate in a wide range of frequencies, covering both the traditional cellular bands, and mm-wave frequency bands, either selecting a specific band or operating in multiple bands simultaneously. For the design of such systems, a detailed understanding of the frequency dependence of the propagation channel is essential. While many channel measurements exist in either microwave bands (< 6 GHz) or near mm-wave bands (> 20 GHz), the results are not easily comparable, and furthermore the transition between these bands is not well studied. This paper aims to bridge the gap by providing the results from a channel measurement campaign conducted in urban macro and micro-cellular environments, over the continuous frequency band of 3–18 GHz.

We characterize the pathloss, shadow fading, Root-Mean-Square (RMS) delay spreads, Ricean factor and coherence bandwidth in urban macro-cellular (UMa) and urban micro-cellular (UMi) environments. Measurements were taken in both line-of-sight (LOS) and non-line-of-sight (NLOS) environments. The pathloss exponents and the RMS delay spreads increase with the Base Station (BS) height in NLOS environment; but not much dependency is observed in the LOS environment. By dividing the wideband channel transfer function into subbands of 1 GHz each, we study the frequency dependence of pathloss, shadow fading, Ricean factor, delay spread, and coherence bandwidth in the 3–18 GHz band. The pathloss exponents vary significantly with frequency, but not-monotonically. The shadow fading and the Ricean factor increase with frequency. The RMS delay spreads decrease with frequency in the LOS environments, but they do not change significantly in the NLOS environments. The coherence bandwidth values do not change significantly with frequency in either environment.

Index Terms—Wideband channel measurements, Delay spreads, Coherence bandwidth

I. INTRODUCTION

With the increasing number of wireless users and applications, mobile data traffic is expected to grow exponentially over the next few years. It is anticipated that fifth generation (5G) wireless systems should be able to support data traffic 1000 times larger than the current, fourth generation (4G), systems [2]. While the majority of the 4G wireless systems operate at frequencies below 6 GHz (henceforth called microwave in this paper), the high data needs motivate expansion to frequency bands above 6 GHz in 5G systems,

as this facilitates use of larger swaths of previously unused spectrum [3], [4]. Furthermore, future systems might either adaptively select an operating frequency band over a wide range, or perform carrier aggregation between the different bands.

The performance of any communication system depends on the propagation channel in which it is operating. Hence it is important to characterize the channel to get a more accurate assessment of the performance of communication systems [5]. While the wireless signal propagation characteristics for the sub 6 GHz frequencies have been well investigated in the literature [5], [6] and references therein, and the majority of the channel measurements motivated by 5G development focused on frequency bands of 20 GHz and above, only few papers have studied the intermediate frequency bands. Refs. [7]–[9] characterize the wireless propagation channel at some discrete frequencies in the 6–20 GHz band (Ref. [7]–[9] at 10 GHz and Ref. [9] at 11 GHz). Only few papers have studied the frequency dependence of the channel transition between microwave frequencies to mm-wave frequencies, which is essential for understanding multi-band and carrier aggregation systems. Ref. [10]–[18] compare the channel propagation characteristics like pathloss and delay spread at the microwave and mm-wave bands, but they measure only a small bandwidth in each band. Also, the majority of these works use different measurement setups for microwave and mm-wave measurements, thereby making the comparison more difficult: for instance, [10] measures frequency bands 10 and 30 GHz; [11], [12] measures frequency bands of 2-4 GHz, 14-16 GHz and 28-30 GHz; [13] measures frequency bands 2.9, 18 and 28 GHz in macro cellular environment; [19] studies the channel propagation characteristics like diffraction and scattering at several discrete frequencies in the 2–60 GHz band in an outdoor environment; [20] studies pathloss at discrete frequencies in the 0.8–37 GHz band in UMi environments; [7] studied RMS delay spreads at 10 and 28 GHz in UMi environments. They all use different channel sounder setups for different subband measurements, and moreover they measure only a small portion of the frequency range. Refs. [21]–[23] summarize the channel measurements done at discrete frequencies in the 6-100 GHz band.

Ref. [14] measured frequency bands 6.5, 10.5, 15 and 19 GHz using the same setup, but the bandwidth is limited to 1 GHz. Moreover, it uses horn antennas with limited azimuth opening and a small elevation beamwidth, thereby limiting the number of interacting scatterers in the environment. The situation is even more complicated for the dependence of the

RMS delay spread on the carrier frequency. It has been often conjectured that the delay spread decreases with increasing carrier frequency, but few experimental proofs have been provided. The situation is compounded by the fact that computation of the delay spread strongly depends on the dynamic range of the receiver. The different measurement setups, and the different pathloss at the various carrier frequencies, make such a comparison very difficult. Yet, this delay spread dependence is critical for the design of 5G cellular systems, as it determines the length of the cyclic prefix, and thus the spectral efficiency of OFDM systems. To the best of our knowledge, there are no continuous wideband measurements that cover both microwave and mm-wave bands. Yet it would be essential since wireless propagation characteristics can be considerably different for microwave and near mm-wave bands as the physical propagation mechanisms like reflection, diffraction and scattering vary as the wavelength changes from a few cm to a few mm.

We partially fill these gaps by performing propagation channel measurements over the continuous frequency band from 3 to 18 GHz in an urban macro-cellular (UMa) and urban micro-cellular (UMi) environment, using the same channel sounder setup. To the best of our knowledge, up to now there are no ultrawideband measurements in the 3 to 18 GHz band reported in the literature for outdoor environment. For the UMa case, we take measurements along different streets in line-of-sight (LOS) and non-line-of-sight (NLOS) environments. For the UMi case, LOS and NLOS measurements were taken for different BS heights. We report the pathloss, shadow fading, root-mean-square (RMS) delay spreads, Ricean factor and coherence bandwidth results for different propagation scenarios and study the dependency of these parameters on the frequency in the 3–18 GHz band. These results considerably expand on the conference version of this paper [1], which focuses on the frequency dependency of delay spread and coherence bandwidth in an UMa environment.

The key contributions of this paper are summarized below:

- For a UMa environment, we provide the pathloss exponents, shadow fading, and RMS delay spreads for the wideband channel, for different measurement routes in LOS and NLOS environments.
- For a UMi environment, we investigate the dependency of the pathloss exponent, shadow fading and RMS delay spreads on the BS height.
- By dividing the wideband channel frequency response into several non-overlapping subbands of 1 GHz bandwidth each, we study the variation of the large scale channel parameters with frequency over the 3–18 GHz band in the LOS and NLOS environments. To enable this study, our measurements apply pre-distortion at the transmitter to ensure (approximately) constant SNR over the measured frequency range, thus eliminating the dynamic range effect from the frequency dependence of the parameters. In particular,
  - We provide the path loss exponents for different subbands in the UMa and UMi LOS/NLOS environments.

- We study the shadow fading variation with frequency and investigate the correlation between the shadow fading in different subbands.
- We study the frequency dependence of the RMS delay spreads, Ricean factor and coherence bandwidth in the 3–18 GHz band.

These large scale channel parameters play an important role in Orthogonal Frequency Division Multiplexing (OFDM) system design [5], which is a key technology used in 4G and 5G communication systems. As a matter of fact, this work was partially motivated by intense discussions in 3GPP about the frequency dependence of the delay spread.

The remainder of the paper is organized the following way: The channel measurement setup is described in Sec. II-A. The measurement environment is described in Sec. II-B. Some general aspects of our data processing are described in Secs. III-A and III-B. For wideband parameters, the data processing is given in Sec. III-C and the pathloss and delay spread results for different measurement scenarios is presented in Sec. IV. For the subband-parameters, the data processing in given in Sec. III-D and the results on the frequency dependency of various channel parameters is provided in Sec. V. A summary and conclusions wrap up the paper in Sec. VI.

II. MEASUREMENT SETUP AND ENVIRONMENT

A. Measurement Setup

Our measurement setup is based on a real time, frequency-hopped, multi-band channel sounder. The transmitter (TX) side comprises of an arbitrary waveform generator (AWG) that generates a multitone complex baseband signal in the 0-1 GHz band with a sampling rate of 1.25 GSps. The 500 MHz inphase and quadrature (I and Q) components of the signal are generated by two channels of the AWG, and upconverted using an IQ mixer to the radio frequency (RF) range, centered around the carrier frequency. A subcarrier spacing of 0.5 MHz was used, which corresponds to a measurable excess path length of 600 m. The RF signal is amplified using a power amplifier and transmitted from a biconical antenna.

At the receiver (RX) end, the signal received by a biconical antenna is passed through a high pass filter (with cutoff frequency at 3 GHz) and low-noise amplifier (LNA). This is done so as to limit the interference from ongoing WiFi and cellular transmissions and to avoid the receiver front end going into saturation. The IQ mixer downconverts the RF signal into baseband, which is then digitized using an analog-to-digital converter (ADC). The transmitter and the receiver setups can be seen in Fig. 1. The azimuth and elevation patterns of the biconical antennas are given in Figs. 2 and 3 respectively. The antennas are isotropic in azimuth and the elevation 3 dB beamwidth decreases from 65 to 45 deg in the 3–18 GHz band. [1]

---

[1]For the azimuth antenna pattern, the ratio of peak to average antenna gain values are respectively 1.16 dB, 0.31 dB, 1.01 dB, 1.36 dB, 1.44 dB and 1.52 dB at frequencies 3 GHz, 6 GHz, 9 GHz, 12 GHz, 15 GHz and 18 GHz. At these frequencies, the respective ratio of peak to average gain values of the elevation antenna pattern are 2.96 dB, 3.14 dB, 2.39 dB, 3.22 dB, 3.43 dB and 3.15 dB.
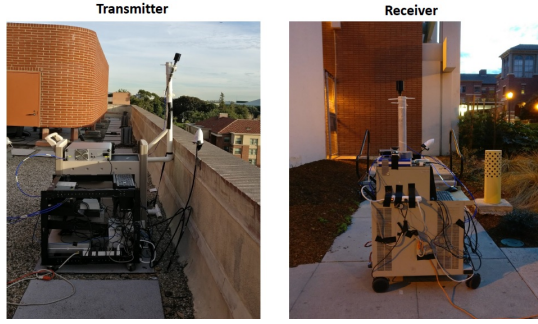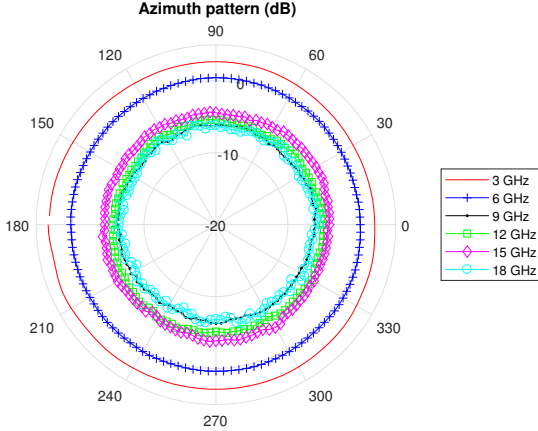
Fig. 1: Transmitter and Receiver setups.

Fig. 2: Azimuth pattern (dB) of the biconical antennas.

Using a combination of frequency synthesizer and frequency reference (one each at the TX and RX), the carrier frequency was varied from 3 GHz to 18 GHz, in steps of 500 MHz. The carrier frequency at the TX and RX are switched in a synchronized way using Labview scripts running on real-time controllers. At any given time, our setup measures the channel frequency response in a 1 GHz subband, centered around the carrier frequency and then switches to the next 1 GHz subband. The successive subband measurements have an overlap of 500 MHz, which is used to correct for the random phase
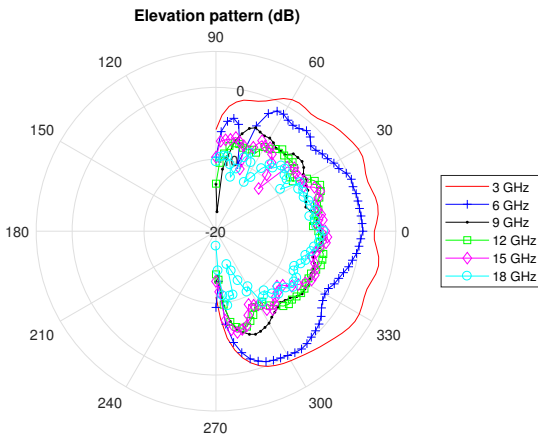

Fig. 3: Elevation pattern (dB) of the biconical antennas.

TABLE I: Minimum and Maximum 3D TX-RX separation distance (in meters) in the UMa environment.

	Route 1	Route 2	Route 3	Route 4
LOS Environment	39m, 117m	48m, 107m	42m, 117m	34m, 101m
NLOS Environment	37m, 97m	70m, 140m	69m, 116m	-

TABLE II: Minimum and Maximum 3D TX-RX separation distance (in meters) in the UMi environment.

	Level 1	Level 2	Level 3
LOS Environment	16m, 79m	18m, 90m	19m, 92m
NLOS Environment	16m, 105m	17m, 102m	18.5m, 107m

shift in the channel transfer function measurements, across the subbands. The phase corrected subband measurements are stitched together to get the wideband channel frequency response in the 3–18 GHz band. The transmit signal is pre-distorted such that the transmit signal-to-noise ratio (SNR) is similar across all subbands. The TX signal power is designed to maintain 40 dBm TX Equivalent Isotropically Radiated Power (EIRP). The only variation in the dynamic range is due to the RX sensitivity. The instantaneous dynamic range of our setup is 53 dB. This varies +/- 1.5 dB across the subbands due to the variations of RX noise figure caused by the LNA noise figure and gain variations. A more detailed description of the channel sounder setup can be found in [24].

The setup takes 100 μs to measure the frequency response in each 1 GHz subband. It takes 100 μs for the setup to switch to the next carrier frequency. Thus, it takes 6 ms to complete the channel measurement in the 3-18 GHz band. We take five such snapshots of the wideband measurements, which is used for noise averaging. The time gap between two successive wide-band measurement snapshots is 10 ms. The multiple snapshots were also used to identify and discard the interference (from the external sources) within the measurement band, which will be described in the next section.

B. Measurement Environment

The measurements were taken near the Electrical Engineering Building (EEB) and the Parking Structure X (PSX) on the USC campus. The density and height of buildings in this area is typical for urban environments. For the EEB location, the transmitter was placed at on the rooftop of the building (of height 29 m) and the receiver was placed on the street, thereby representing a typical macro-cellular setup. For the PSX measurements, the transmitter was placed on different levels of the building (of height 12.5 m) and the receiver on the street, thereby representing a typical micro-cellular setup.

UMa measurements: The transmitter was placed at two different locations on the rooftop of EEB and the receiver setup was placed on a cart and moved along McClintock and 37th Street. The measurement routes along with the TX locations are shown in Fig. 4 and 5, respectively, for the LOS and NLOS measurements. The lamp posts, parking meters, cars parked along the sidewalks, and the buildings on either side of the measurement routes provide a rich scattering environment. The

Fig. 4: LOS routes for the UMa measurements.

Fig. 5: NLOS routes for the UMa measurements.

TX antenna was effectively 31 m above the ground and the RX antenna was 1.5 m above the ground. The transmitter was surrounded by buildings of height 20–30 m. The streets were roughly 15 m wide and the length of the measurement routes varied from 70 m to 120 m. The minimum and maximum TX-RX separation distance for different measurement routes is provided in Tab. I. For the LOS measurements, first the TX was placed at the corner of the rooftop and the RX was moved along the perpendicular streets (route 1 and 2); the TX was then placed at the center of the building and the RX moved along 37th street (route 3 and 4), thereby generating 4 realizations of the LOS measurement routes. For the measurement route 1, the receiver was moved along the center of the street and there was clear LOS for all the measurement locations along the route. For measurement routes 2, 3 and 4, the receiver was moved along the sidewalk covered with trees and occasionally the LOS path was obstructed by foliage. The transmit antenna was down-tilted by 15 degrees so that for the majority of the measurement points along the routes, the geometrical LOS component is within the half power elevation beamwidth of the TX antenna.

A similar procedure was repeated for the NLOS measurements. The TX was first placed at the corner and the RX was moved along the perpendicular streets (route 1 and 2); the TX was then placed at the center and the RX was moved along the McClintock street (route 3), thereby generating 3 realizations of the NLOS measurement routes.

UMi measurements: The TX was placed on three different levels of the parking structure, very close to the outside wall; since the structure has large openings to the exterior, the TX antenna was essentially at a location where a wall-mounted microcell antenna would be on a regular building. The RX was moved along one LOS route and one NLOS route as shown in

Fig. 6: LOS and NLOS routes for the UMi measurements.

Fig. 6. The TX antenna was effectively 8.5 m, 11.5 m and 14 m for the BS on level 1, 2, and 3 respectively. The RX antenna was 1.5 m above the ground. The transmitter was surrounded by buildings of height 15–30 m. The streets were 12 m wide. The length of the LOS and NLOS measurement route was 90 m and 65 m, respectively. The minimum and maximum TX-RX separation distance for different measurement routes is provided in Tab. II. For all the TX-RX location pairs, the elevation angle of the geometric LOS component is well within the 3 dB elevation beamwidth of TX antenna, thereby reducing the impact of different elevation beamwidths at different frequencies. No tilt was applied to the transmit or receive antennas for the UMi measurements.

III. Data processing

For each measurement route, the receiver cart was moved continuously along the street, roughly at a speed of 0.2 m/s. Measurements were taken every 1 s and in each measurement, our setup records five snapshots of the channel impulse response, with a time gap of 10 ms between successive snapshots.

A. Noise averaging and Interference filtering

The multiple snapshots can be used for noise averaging and interference suppression, since the first and the last (fifth) snapshots have time gap of 40 ms, which corresponds to 0.8 cm spacing; equivalent to 0.08λ spacing at 3 GHz carrier frequency and 0.48λ at 18 GHz carrier frequency. Thus, the multiple snapshots will experience similar small scale fading and hence can be used for noise averaging. [2]

The multiple snapshots can also be used to suppress the bursty WiFi interference. Occasionally, for some of the measurement routes, we noticed interference from WiFi access points operating in the 5 GHz band. Since the interference might be present only in a subset of the snapshots, using a pairwise correlation of the snapshot channel impulse responses, followed by median filtering, we can discard the snapshots

---

[2]For the higher frequency subband measurements, the SNR gain from averaging the snapshots was observed to be 5–6 dB. It is 1–2 dB smaller than the expected theoretical value of 7 dB. This is because of some signal variations across the averaging distance at higher frequencies.

corrupted by interference [25].[3] The remaining snapshots are used for noise averaging.

B. Small scale fading averaging

Since the measurements were taken every 1 s along the route, this corresponds to 0.2 m spacing between the successive measurements; equivalent to 2λ spacing at 3 GHz carrier frequency and 12λ at 18 GHz carrier frequency. Thus, the successive measurements along the route will experience independent small scale fading and hence can be used for spatial averaging to compute the large scale channel parameters like pathloss, delay spreads, coherence bandwidth, etc.

C. Wideband Processing

1) Averaged Power Delay Profile (APDP) computation: Let $\{H_T(f_k), k = 1 \cdots N_F\}$ be the wideband channel frequency response[4] measured at time T seconds (time is measured relative to the first measurement in that route). For our measurement setup, $f_1 = 3$ GHz, $\Delta f = f_2 - f_1 = 0.5$ MHz and $N_F = 30000$. The channel frequency response is transformed to the delay domain by taking an IFFT with a Hann window to suppress the sidelobes. Let $h_T(\tau)$ denote the resulting channel impulse response. The magnitude squared of the impulse response gives the instantaneous power delay profile, $PDP_T(\tau)$. The influence of the small scale fading is removed by averaging the consecutive instantaneous PDP measurements within a window, to get the averaged power delay profile (APDP). Here the averaging window is defined as the set of consecutive measurements where the multipath component (MPC) path powers are similar, but the phases of the MPCs change across measurements. This is characterized using the correlation between the instantaneous PDP and the variation in the overall received power. To put it mathematically,

$$APDP(\tau) = \frac{1}{N} \sum_{T=k}^{k+N} |h_T(\tau)|^2 \tag{1}$$

where $N \triangleq \min(N_1, N_2)$. N_1 denotes the number of consecutive measurements over which the PDP's are correlated and N_2 denotes the number of consecutive measurements whose received power does not vary by more than 3 dB.

$$N_1 = \min\{n : Corr(PDP_k(\tau), PDP_{k+n}(\tau)) < 0.5\} \tag{2}$$

$$N_2 = \min\{n : |P_k - P_{k+n}| > 3\ dB\} \tag{3}$$

---

[3]This approach does not work if all the snapshots are corrupted by interference. In such a case, we use the power variations in the subbands to detect and discard the measurements with interference. We divide the wideband channel frequency response into subbands of 300 MHz and look at the power variations across the subbands. If there is a large jump in the received power in adjacent subbands (in excess of 10 dB), it is probably because of the interference and hence we discard such measurements for further processing.

[4]We treat the antennas as a part of the channel, as the antenna response cannot be clearly separated from the overall response. We take a reference measurement by replacing the TX and RX antennas and connecting the transmitter and receiver setup with a cable. The cable has been calibrated and its response has been taken out from the reference measurement. We then divide the overall system response with the reference measurement, to get the true response of the channel and the antennas. Calibrated antenna arrays at TX and RX would be required to eliminate the impact of antennas.
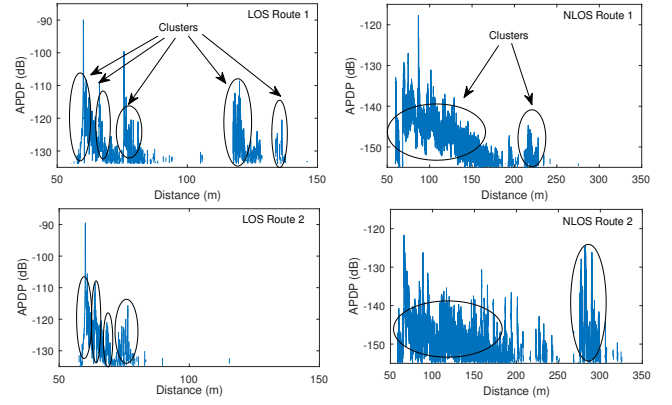

Fig. 7: Sample APDP plots for measurement taken along different routes in the UMa LOS and NLOS environments.

where $Corr(.,.)$ denotes the correlation coefficient and $P_T = 10 \log_{10} \left(\sum_{k=1}^{N_F} |H_T(f_k)|^2 \right)$ denotes the power in the channel frequency response.

Due to the extremely high delay resolution, even movement over short distances can lead to noticeable delay changes. To reduce the impact caused by this, the impulse responses are time adjusted such that the strongest MPC is time-aligned. To reduce the effects of noise, we subtract the average noise power level from the APDP, and a noise-thresholding filter is applied to the resulting APDP, in which the APDP samples whose magnitude is below a threshold is set to zero. The threshold is set to be 6 dB above the noise floor. The noise floor is computed from the noise-only region of the APDP (samples before the first MPC). This APDP is used to compute the RMS delay spread and the coherence bandwidth of the channel.

Fig. 7 plots sample APDPs for the measurements taken along Routes 1 and 2 in LOS and NLOS environments. For the LOS measurement routes, we typically observe 3-5 clusters, depending on the measurement route. The maximum number of clusters was observed for measurement route 1. For this route, apart from the LOS cluster, we observed far away clusters resulting from reflection from building P, located at the end of the measurement route. For the NLOS measurement routes, there were typically 1-2 clusters. We conjecture that these might be due to "merging" of different clusters, and resolution in directional domains would give a higher number.

2) Wideband Pathloss and shadow fading characterization: The path gain (inverse of the pathloss) is obtained by averaging the absolute magnitude squared of the channel frequency response over the small scale fading realizations and averaging this quantity over frequency. [5]

$$PL(d) = 10\alpha \log_{10}\left(\frac{d}{1\ m}\right) + \beta + S_\sigma \tag{4}$$

---

[5]The pathloss definition used here is equivalent to the "transmission loss" definition of ITU-R.

where $PL(d)$ denotes the pathloss (measured in dB) at TX-RX separation distance d; β is an offset and α is referred as a pathloss exponent; S_σ is a shadow fading term that captures the deviation of the measured pathloss from the linear model. This is typically modeled using a zero-mean normal distribution with a standard deviation σ. As with all measurement-based fitting models, the result is only valid in the distance range in which the measurements were made.

3) Wideband Delay spread: The RMS delay spreads are computed as the second central moment of the APDP [5].

$$\tau_{RMS} = \sqrt{\frac{\int_0^\infty (\tau - \bar{\tau})^2 \, APDP(\tau) \, d\tau}{\int_0^\infty APDP(\tau) \, d\tau}} \qquad (5)$$

where $\bar{\tau}$ is the mean delay, which is given by

$$\bar{\tau} = \frac{\int_0^\infty \tau \, APDP(\tau) \, d\tau}{\int_0^\infty APDP(\tau) \, d\tau} \qquad (6)$$

D. Subband Processing

We now study the frequency dependency of the large scale channel parameters in the 3–18 GHz band. We divide the measured wideband channel frequency response into 15 non-overlapping subbands (3-4 GHz, 4-5 GHz, $\cdots$, 17-18 GHz) with each subband bandwidth equal to 1 GHz. Similar approach of subband processing was also used in [26]. The APDP processing described above is repeated for each of the subbands and the pathloss exponents, shadow fading and RMS delay spreads are independently computed for each of these subbands. For a fair comparison, we make sure that the number of realizations used for small scale fading averaging is the same across all subbands. Since the value of N can be different for different subbands, we compute N for each of the 15 subbands and pick the minimum value across the subbands. [6]

1) Ricean factor: The Ricean factor is defined as the ratio of the power in the dominant MPC to all other MPCs. It is an important parameter in characterizing the propagation channel in LOS environments. For narrowband channels, it is computed using the classical method of moments [27]. This approach has been extended to wideband channels, by interpreting the signals on different subcarriers as different narrowband fading realizations [28]. Thus, the Ricean factor in each subband is computed as follows:

$$G_a = \frac{1}{n} \sum_{i=1}^n |H_i|^2 \qquad (7)$$

$$G_v = \frac{1}{n-1} \left(\sum_{i=1}^n |H_i|^4 - n G_a^2 \right) \qquad (8)$$

$$K = \frac{\sqrt{G_a^2 - G_v}}{G_a - \sqrt{G_a^2 - G_v}} \qquad (9)$$

where $\{H_i\}_{i=1}^n$ are the channel frequency responses measured at n frequencies, spaced apart by coherence bandwidth, and hence provide n different narrowband fading realizations.

---

[6]For the data, N varied from 4 to 10, with an average value of 8.

TABLE III: Standard deviation of shadow fading in the UMa environment (dB).

	Route 1	Route 2	Route 3	Route 4
LOS Environment	0.27	0.17	0.62	0.55
NLOS Environment	1.89	1.02	1.43	-

Since the number of spatial small scale fading realizations of H in each averaging window is small (typically 4 to 10), we pick the realizations of H that are spaced apart by a coherence bandwidth and combine them all into a single ensemble for Ricean factor computation.[7] Note that picking uncorrelated values of fading realizations is important to avoid bias in the estimation of the Rice factor [28].

2) Coherence Bandwidth: The channel coherence bandwidth for each subband is computed using the frequency correlation function, which is obtained by taking the Fourier transform of the corresponding subband APDP. The 3 dB coherence bandwidth is the smallest frequency at which the magnitude of the correlation function becomes less than half of the maximum value.

$$BW_{0.5} = \min \left\{ \Delta f : \left| \frac{S(\Delta f)}{S(0)} \right| < 0.5 \right\} \qquad (10)$$

IV. WIDEBAND MEASUREMENT RESULTS

A. Wideband Pathloss and Shadow fading

Fig. 8 plots the measured pathloss values along different measurement routes in the UMa LOS/NLOS environments. In the LOS environment, the pathloss exponent was close to 2 for the receiver on route 1, 2 and 4, and it was observed to be less than 2 for the receiver on route 3, indicating strong waveguiding. In the NLOS environment, the pathloss exponents were observed to be significantly different for the RX along different measurement routes (varying from 2.71 to 4.34), which is consistent with other recent results; compare [29], which also provides a discussion of the reasons.

We now compare the measured pathloss exponents with the values specified in the 3GPP standards [30], for similar propagation scenarios. In the UMa LOS environment, the measured pathloss values are comparable with the pathloss exponent of 2.0, specified for similar TX-RX separation distances and for similar carrier frequencies. In the UMa NLOS environment, the specified pathloss value is 3.92. This is comparable to the measured pathloss values of 4.24 and 4.34 for two of the measurement routes. In the UMi environment, pathloss exponents of 2.1 and 3.2 were specified for the LOS and NLOS environments. The measured pathloss exponents (1.54–1.93 in LOS and 2.22–2.80 in NLOS) were somewhat smaller than values specified in the 3GPP.

The standard deviation of the shadow fading for various measurement scenarios in the UMa environment is listed in Table III. As expected, the shadowing standard deviation values are higher for the NLOS environment.

Fig. 9 plots the measured pathloss values for different BS heights in the UMi LOS/NLOS environments. In the LOS

---

[7]Based on the results in Sec. V-E, the typical coherence bandwidth values are 200 MHz. Since each subband is 1 GHz wide, this approach increases the sample size by a factor of 5.
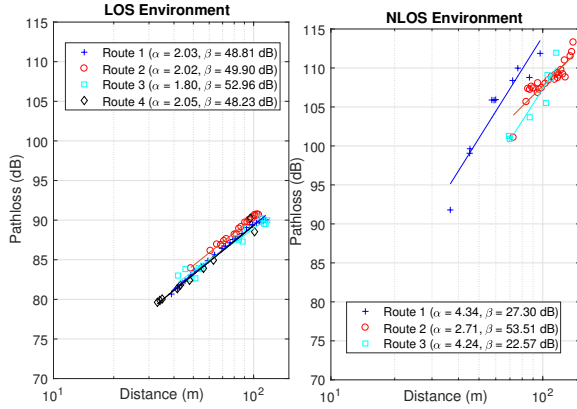
Fig. 8: Distance dependent pathloss in the LOS and NLOS environments for the UMa measurements. The 95% confidence intervals for the least square fit in LOS environments are: [1.96, 2.09], [1.94, 2.10], [1.62, 1.97], and [1.85, 2.25] for measurements routes 1, 2, 3 and 4 respectively. The corresponding intervals in NLOS environment are: [3.40, 5.27], [2.23, 3.18], and [2.85, 5.62] for measurement routes 1, 2 and 3 respectively.
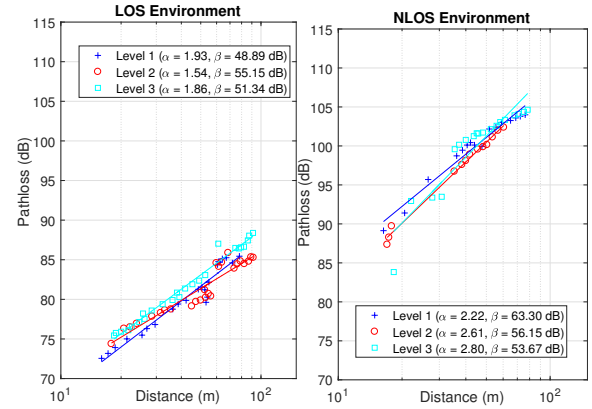

Fig. 9: Distance dependent pathloss in the LOS and NLOS environments for the UMi measurements. The 95% confidence intervals for the least square fit in LOS environments are: [1.75, 2.10], [1.36, 1.72], and [1.77, 1.96] for BS on level 1, 2, and 3 respectively. The corresponding intervals in NLOS environment are: [2.02, 2.42], [2.48, 2.72], and [2.32, 3.27] for BS on level 1, 2 and 3 respectively.

TABLE IV: Standard deviation of shadow fading in the UMi environment (dB).

	Level 1	Level 2	Level 3
LOS Environment	1.27	1.10	0.61
NLOS Environment	0.83	1.03	1.90

environment, there is no clear pattern in the pathloss exponent variation with the BS height. But in the NLOS environment, the pathloss exponents seem to increase as the BS height increases and the pathloss exponents are smaller than the ones in the UMa environment. The standard deviation of the shadow fading for different BS heights in the UMi environment is listed in Table IV. In the LOS environment, the shadowing values seem to decrease as the BS height increases. The shadowing increases with the BS height in the NLOS environment. The observed behavior can be explained as follows. In the LOS environment, as the BS height increases, the LOS path becomes more dominant due to reduced scattering around the BS and hence the shadow fading decreases with the increase in BS height. In the NLOS environment, as the BS height increases, it can potentially illuminate a larger area and hence the increased scattering results in increased shadow fading.

B. Wideband RMS delay spread

Fig. 10 plots the CDF of the measured wideband RMS delay spread (ns values) for different measurement routes in the LOS/NLOS UMa environments. The delay spreads are in the range of 20–60 ns in the LOS environment and 60–300 ns in the NLOS environment. It can be seen that the log values of the delay spreads fit well with a Normal distribution. The parameters of the distribution (mean μ and standard deviation σ) are given in the legend. The CDF curves are significantly different for different measurement routes both in LOS and
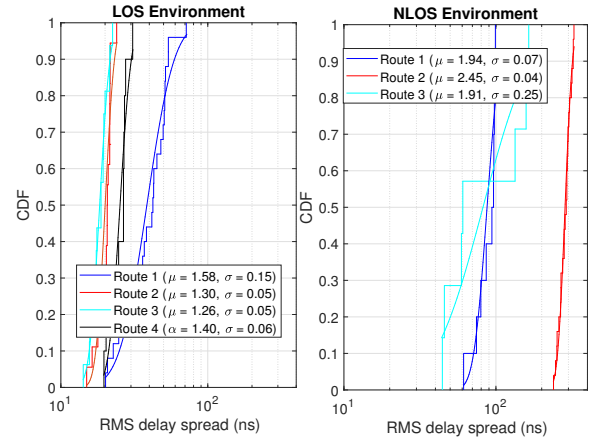

Fig. 10: CDF of RMS delay spreads (ns) for different measurement routes in the UMa environment.

NLOS environments, except that for route 2 and 3 in the LOS environment, which are in the same street with only the TX location different.

Fig. 11 compares the CDF of the measured wideband RMS delay spread (ns) for different BS heights in the LOS/NLOS UMi environments. The delay spreads are in the range of 25–50 ns in the LOS environment and 30–140 ns in the NLOS environment. While the delay spreads are comparable to the UMa case in the LOS environment, they are significantly smaller when compared to UMa case in the NLOS environment. This is again intuitive, as a UMi BS cannot effectively illuminate far scatterers, so that long-delayed echoes carry less power than in the UMa case. It can be seen that the log values of the delay spreads fit reasonably well to a Normal
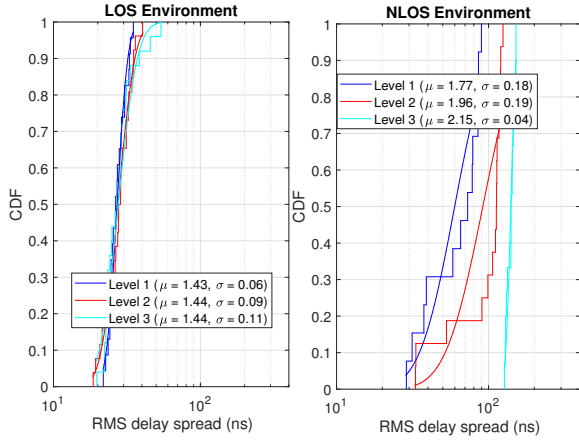
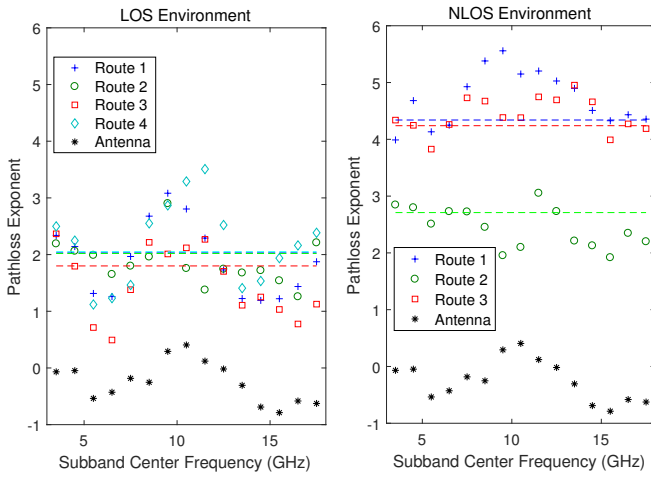Fig. 11: CDF of the RMS delay spreads (ns) for different BS heights in the UMi environment.

Fig. 12: Pathloss exponents as a function of the frequency for different measurement routes in the UMa LOS/NLOS environments.

distribution.[8] While the delay spreads do not change much with the BS height in the LOS environment, they increase with increasing BS height in the NLOS environment.

V. Subband Measurement Results

A. Subband Pathloss characterization

Fig. 12 plots the pathloss exponents as a function of the subband center frequency for the UMa LOS and NLOS environments. The corresponding wideband pathloss exponents for each of the measurement routes are marked using dotted lines. In the LOS environment, it can be seen that there are large variations in the pathloss exponents over the subbands,

[8]While the log-Normal distribution is not a good fit for some of the measurement routes in the NLOS scenario, we still use a log-Normal distribution because (i) this distribution has been used extensively in the literature and standardized channel models, (ii) using the same distribution for all routes allows an easier comparison, and (iii) due to the small sample size, establishing statistical validity of a different distribution would be difficult.
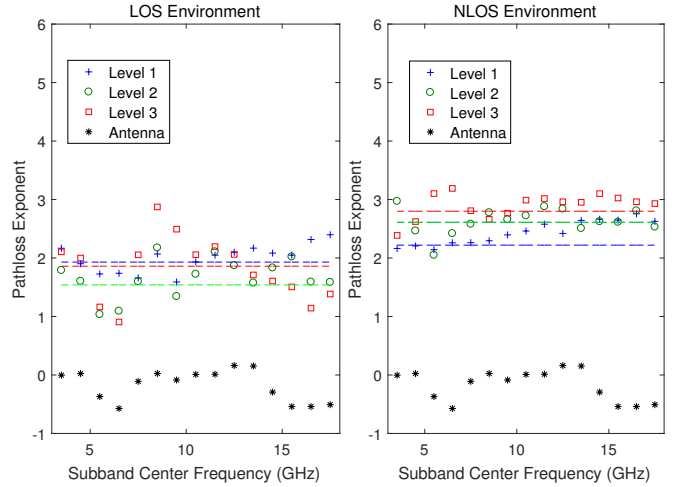

Fig. 13: Pathloss exponents as a function of the frequency for different BS heights in the UMi LOS/NLOS environments.

which are more or less consistent across different measurement routes–pathloss exponents are close to 2 in the 3–5 GHz band; decreases to 1 in the 5–8 GHz band; vary between 2 and 3 in the 8-13 GHz band; and between 1 and 2 in the 13–18 GHz band. We conjecture that a part of these variations is caused by the antennas. Specifically, while the antennas are omnidirectional in azimuth at all frequencies, and the antenna gain (in the horizontal plane) does not vary appreciably with the azimuth angle, the shape of the antenna elevation pattern is different for different frequencies. The elevation and azimuth gain patterns of the antennas, for different subbands, has been measured inside the anechoic chamber at USC.

As the RX moves along the street, the elevation angle corresponding to geometric LOS between the TX and RX decreases from 45 deg to 5 deg. Since the antennas are not isotropic in the elevation domain as outlined above, the effective gain of the TX and the RX antennas changes with the elevation angle, and equivalently with the TX-RX separation distance. Thus the antenna response itself has an effective distance dependence, which is different for different frequency bands as shown in Fig. 12, the frequency dependence induced on the pathloss coefficient by the antenna response (black star). Note that while the general trend in the pathloss exponent variation with frequency for the measured channel, follows the antenna response, the magnitude of the variation is increased for the measured channel, thereby indicating different pathloss exponents for different subbands for the propagation channel alone.

In the UMa NLOS environment, there is large variation in the pathloss exponents over the subbands and it is different for different measurement routes, and also different from the antenna response. In the NLOS environment, there is no dominant LOS component; MPCs incident at different elevation angles will have comparable power and hence the impact of antenna response is more likely to be averaged out.

Fig. 13 plots the pathloss exponents as a function of the subband center frequency for the UMi LOS and NLOS
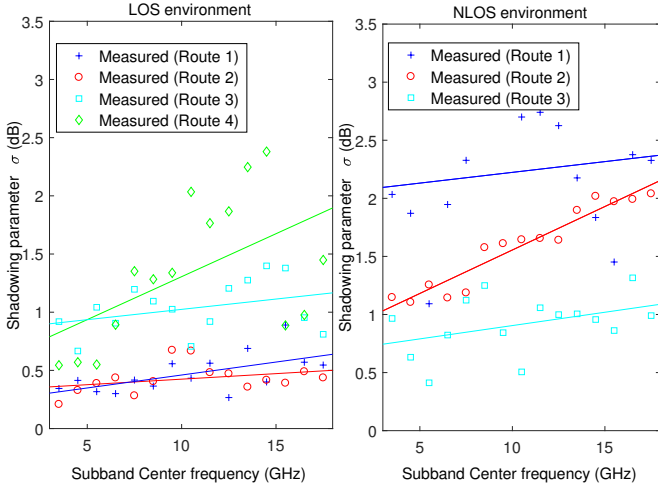
Fig. 14: Shadow fading as a function of the frequency for different measurement routes in the UMa LOS/NLOS environments.

Fig. 15: Shadow fading as a function of the frequency for different BS heights in the UMi LOS/NLOS environments.

environments. The observations are similar as in the UMa case. For the LOS environment, the pathloss exponents vary significantly across the subbands and it can be explained by the variation in the antenna response. The pathloss exponents are similar for different BS heights in the majority of the subbands. In the NLOS environment, it can be seen that the subband pathloss exponents roughly increase with frequency. The subband pathloss exponents increase with the increase in the BS height, which is consistent with our earlier observations on the wideband pathloss exponents variation with the BS height. Also, these pathloss exponents are smaller than the ones observed in UMa environment, where the BS height is even larger.

It can be seen that, in general, the wideband pathloss exponents are close to the subband pathloss exponents obtained in the lower end of the 3–18 GHz band. This is because of the relatively large antenna gain at lower frequencies.

Similar observations on the subband pathloss exponent variation with frequency was reported in [31]. In the UMi environment, the reference provides the pathloss exponents measured at four discrete frequencies of 3.5 GHz, 5.2 GHz, 10 GHz and 18 GHz in the 3–18 GHz band. In the UMi LOS environment the pathloss exponents varied between 1.9 and 2.5 and in the UMi NLOS environment they varied between 3.5 and 4.1 with no clear pattern in the variation with frequency. For the UMa environment, the pathloss exponents were reported at two discrete frequencies of 10 and 18 GHz in the 3–18 GHz band. In the UMa LOS environment the pathloss exponents varied between 2.0 and 2.1 and in the UMa NLOS environment they varied between 3.3 and 4.9.

B. Subband shadow fading characterization

Fig. 14 and 15 respectively plot the shadow fading as a function of the subband center frequency in the UMa and UMi environments. It can be seen that for both the UMa and UMi scenarios, the shadow fading standard deviation seems to
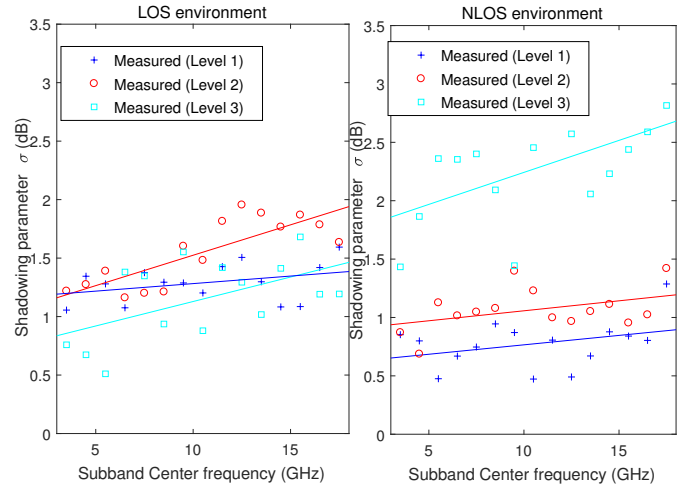
increase with the frequency. In the UMi NLOS environment, the shadow fading increases with the BS height. As the BS height increases, it can potentially illuminate a larger areas and hence the increased scattering results in increased shadow fading. [9]

The measured shadow fading values are smaller than the values reported in [31]. In the UMi LOS environment the shadow fading values varied between 3.1 dB and 5.4 dB and in the UMi NLOS environment they varied between 8.3 dB and 9.2 dB with no clear pattern in the variation with frequency. In the UMa LOS environment the shadow fading values varied between 4.7 dB and 5.1 dB and in the UMi NLOS environment they varied between 4.5 dB and 7.8 dB. For these reported measurements, the TX-RX separation distance was varied from 100 m to 1000 m. The higher shadow fading values were probably because of computing the pathloss exponent and shadow fading by combining the measurements done over several streets. In our measurements, we fit the pathloss and shadow fading for each street separately and hence smaller shadow fading values. Also, shadow fading tends to increase with distance.

The differences in the behavior and the magnitude of shadow fading values is probably because our measurements were confined to a smaller area, thereby illuminating relatively smaller number of scatterers and hence smaller shadowing values. Shadow fading tends to increase with distance.

We also investigate the correlation of the shadow fading across different subbands. For this we combine the shadow fading realizations across different measurement

[9]We investigated the impact of antenna pattern on the shadow fading values and observed that it is quite small. In the LOS environment, since most of the scatterers are illuminated within the 3 dB elevation beamwidth of the TX antenna, the power variation with distance due to the antenna pattern is small. For each subband, we computed the shadow fading caused by the antenna pattern. The standard deviation of the shadow fading was small (less than 0.4 dB) compared to the measured shadow fading values. In the NLOS environment, multipaths incident at different elevation angles will contribute significantly to the overall received power and hence the impact of antenna pattern will be averaged out.
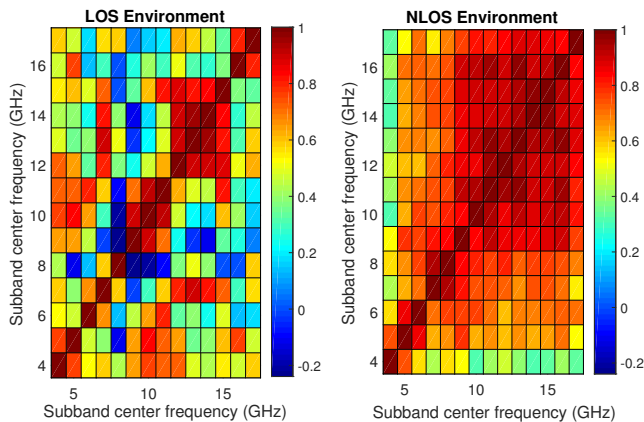
Fig. 16: Correlation matrix of the shadow fading across different subbands in the UMa LOS/NLOS environments.
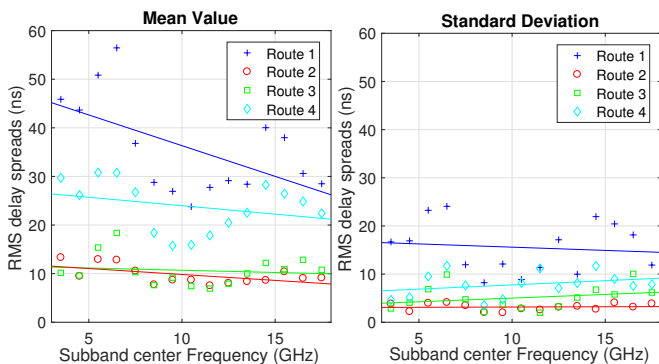

Fig. 17: Mean and standard deviation of the RMS delay spreads (ns), for different subbands, in the UMa LOS environment. The 95% confidence intervals for the slope (mean value plot): $[-2.14, -0.37]$, $[-0.41, -0.07]$, $[-0.42, 0.14]$, and $[-0.89, 0.09]$ for measurements routes 1, 2, 3 and 4 respectively. The corresponding intervals for standard deviation plot are: $[-0.71, 0.44]$, $[-0.06, 0.09]$, $[-0.12, 0.42]$, and $[-0.19, 0.42]$.

routes. Fig. 16 captures the pairwise correlation of shadow fading across different subbands in the UMa LOS and NLOS environments. It is interesting to see that at the higher ends of the 3–18 GHz bands, shadow fading is more correlated with the adjacent bands. This behavior is more prominent in the NLOS environment. This behavior is especially interesting in view of multi-band systems, which often rely on uncorrelated shadowing at different subbands. As a matter of fact the current 3GPP channel model assumes completely independent shadowing in different frequency bands, an assumption that is not supported by our measurements.

C. Subband RMS delay spreads characterization

We now study the frequency dependency of the RMS delay spreads in the 3–18 GHz band. Since the wideband RMS delay spreads are observed to be significantly different for different measurement routes, we do not combine the subband data
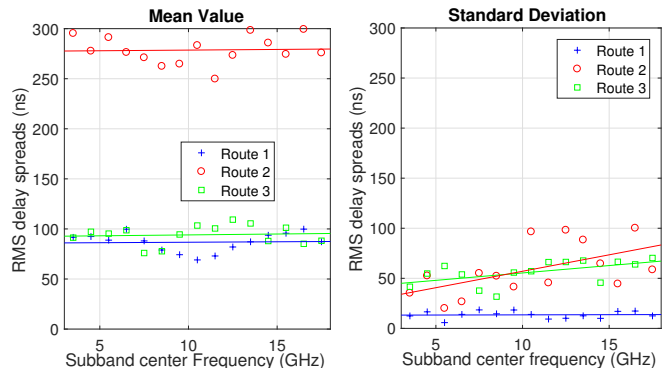

Fig. 18: Mean and standard deviation of the RMS delay spreads (ns), for different subbands, in the UMa NLOS environment. The 95% confidence intervals for the slope (mean value plot): $[-0.95, 1.13]$, $[-1.40, 1.66]$, and $[-0.34, 1.59]$ for measurements routes 1, 2, and 3 respectively. The corresponding intervals for standard deviation plot are: $[-0.37, 0.43]$, $[0.92, 5.63]$, and $[0.38, 2.57]$.

across different measurement routes, but rather analyze each measurement route separately.

In the LOS environment, it is observed that the delay spreads decrease from 3 GHz to 18 GHz. For instance, in measurement route 1, the mean delay spreads decreases from 46 ns for 3–4 GHz band to 29 ns for 17–18 GHz band.[10] The standard deviation of the delay spreads only changes by few ns across the subbands.

Fig. 17 plots the mean and standard deviation of the RMS delay spreads (ns) as a function of the subband center frequency for the measurement routes in the UMa LOS environments. It can be seen that, for the majority of the measurement routes, the mean decreases with frequency and the standard deviation only changes by only few ns with frequency. This is also supported by the 95% confidence interval of the slopes. This behavior can be explained as follows: Blockage is more severe at higher frequencies, since diffraction is a less efficient process. While the power in both the LOS and non-LOS MPCs decreases with frequency, the decrease is relatively stronger for the non-LOS MPCs, thereby resulting in decreasing delay spreads with increasing frequency. This can also be seen from the sample APDP plots for different subbands in Fig. 21. The figure compares the normalized APDP for different subbands in UMa LOS. The subband APDP is normalized by the total power in that subband. While the power in the LOS component is very similar, for the NLOS component at 50 m delay, the power reduces from -13 dB (3–4 GHz band) to -16 dB (7–8 GHz band) and to -20 dB (11–12 GHz band). Similarly for the NLOS component at 42 m delay, the power reduces from -17 dB (3–4 GHz band) to -21 dB (7–8 GHz band) and to

---

[10]The RMS delay spreads of the antenna response varied from 2 ns to 8 ns across different subbands and elevation angles. Since this is significantly smaller than the channel delay spreads, we can conclude that the variation in the delay spreads here are purely because of the propagation channel. This is somewhat in contradiction to the observations made in Ref. [7]. There it was observed that the RMS delay spreads did not change much from 10 GHz to 28 GHz.
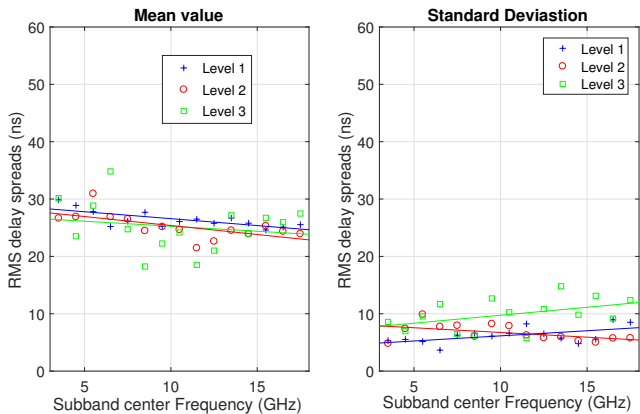
Fig. 19: Mean and standard deviation of the RMS delay spreads (ns), for different subbands, in the UMi LOS environment. The 95% confidence intervals for the slope (mean value plot): $[-0.33, -0.02]$, $[-0.50, -0.12]$, and $[-0.64, 0.22]$ for BS on level 1, 2, and 3 respectively. The corresponding intervals for standard deviation plot are: $[0.04, 0.31]$, $[-0.30, -0.02]$, and $[0.17, 1.11]$.
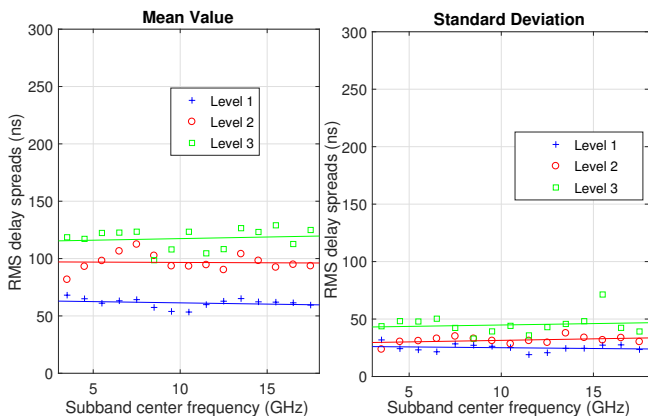

Fig. 20: Mean and standard deviation of the RMS delay spreads (ns), for different subbands, in the UMi NLOS environment. The 95% confidence intervals for the slope (mean value plot): $[-0.87, 0.75]$, $[-0.89, 0.24]$, and $[-0.70, 1.26]$ for BS on level 1, 2, and 3 respectively. The corresponding intervals for standard deviation plot are: $[-0.06, 0.39]$, $[-0.48, 0.21]$, and $[-0.70, 1.19]$.

-22 dB (11–12 GHz band).

Fig. 18 plots the mean and standard deviation values as a function of the subband center frequency for the measurement routes in the UMa NLOS environments. Unlike the LOS case, here the mean neither decreases nor increases with frequency but the standard deviation shows increase with frequency for two out of three measurement routes. At higher ends of the 3–18 GHz band, the wavelength (few mm) will be comparable to roughness of the scatterers in the environment, thereby making the received power from the scattering relatively more sensitive to frequency. Since, there is no single dominant propagation path, the received power is contributed by multiple scatterers.
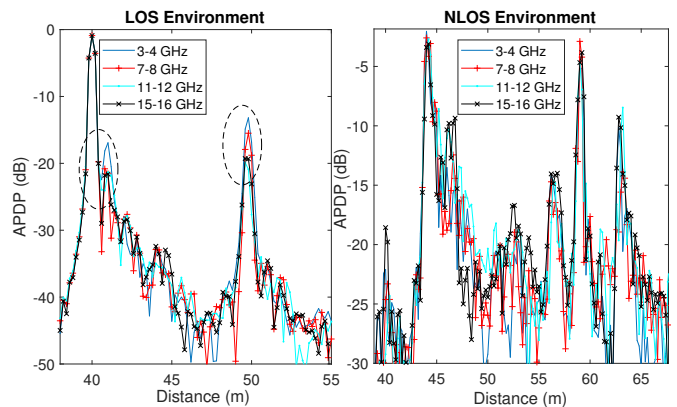

Fig. 21: APDP (normalized by received power) for different subbands in UMa LOS and NLOS environments.

Different multipaths can have different magnitude of power variation with frequency, thereby resulting in increased variance of RMS delay spreads with frequency. This can also be seen from Fig. 21 which plots the sample APDP for different subbands in NLOS UMa environment. In each subband, the APDP is normalized with the total power in that subband.

Figs. 19 and 20 plot the mean and standard deviation values as a function of the subband center frequency for the measurements taken with different BS heights in the UMi LOS and NLOS environments respectively. In the LOS environment, for the majority of the measurement routes, the mean delay spreads decreases with frequency. The subband delay spreads do not change with the BS height. In the NLOS environment, the mean and the standard deviation neither increase nor decrease with the frequency, but the RMS delay spreads increase with the increase in the BS height. These subband delay spread variations with the BS height are consistent with our earlier observations on the wideband delay spread results.

D. Subband Ricean factor characterization

We now study the Ricean-K-factor dependency on the frequency. The K-factor in each 1 GHz subband is computed as described in Sec. III-D1. In each subband, we fit the measured dB values of the Ricean-K-factor using the Normal distribution. Fig. 22 plots the mean and standard deviation of the K-factor as a function of frequency, for different measurement routes in the UMa LOS environment. It can be seen that the K-factor increases with frequency. This can be explained as follows: while the power in both the LOS and non-LOS MPCs decreases with frequency, the decrease is stronger for the non-LOS MPCs, thereby resulting in larger K values with increasing frequency. This can also be seen from the sample APDP plot in Fig. 21.

Similar observations hold true even in the UMi LOS environment as can be seen from Fig. 23. Mean and standard deviation values are given for different BS heights. The K-factor increases with frequency. The mean K-factor values increased as the BS moved from level 1 to level 3. This
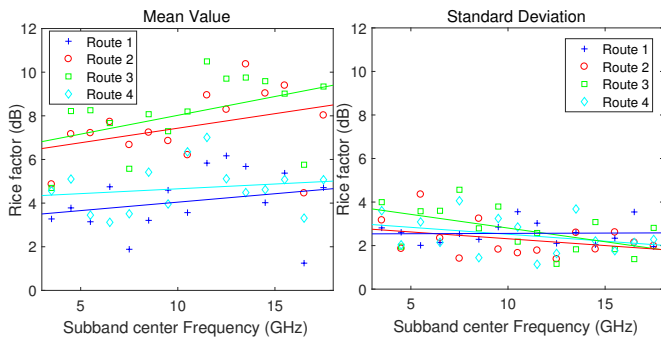
Fig. 22: Mean and standard deviation of the Ricean factor (dB) for different subbands in the UMa LOS environment. The 95% confidence intervals for the slope (mean value plot): $[-0.07, 0.23]$, $[0.02, 0.29]$, $[0.01, 0.33]$, and $[-0.05, 0.17]$ for route 1, 2, 3, and 4 respectively.

Fig. 24: Mean and standard deviation of the Coherence bandwidth (MHz) for different subbands in the UMa LOS environments. The 95% confidence intervals for the slope (mean value plot): $[-1.07, 4.08]$, $[0.77, 1.99]$, $[0.17, 1.68]$, and $[-3.52, 4.52]$ for route 1, 2, 3, and 4 respectively.
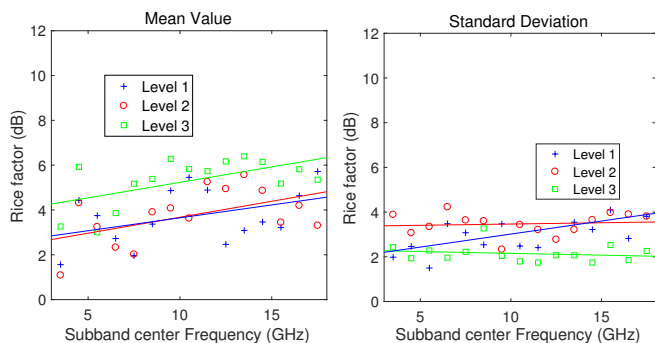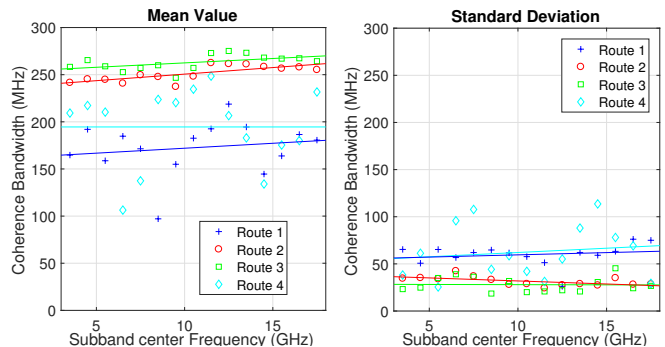

Fig. 23: Mean and standard deviation of the Ricean factor (dB) for different subbands in the UMi LOS environment. The 95% confidence intervals for the slope (mean value plot): $[-0.09, 0.29]$, $[-0.05, 0.22]$, and $[-0.06, 0.20]$ for the BS on level 1, 2, and 3 respectively.

E. Subband Coherence Bandwidth characterization

We now investigate the coherence bandwidth dependency on the subband center frequency. While there is a common misconception that the coherence bandwidth is simply the inverse of the RMS delay spread, this is not true–the two quantities are characterized by an uncertainty (inequality) relationship [33], and thus their frequency dependence might be different. We compute the coherence bandwidth in each 1 GHz subband, as described in Sec. III-D2. We investigate the frequency dependency by studying the variation of the mean and standard deviation values with frequency.

Fig. 24 plots the mean and standard deviation of the coherence bandwidth (MHz) as a function of the subband center frequency, for different measurement routes in the UMa LOS environment. In the LOS environment, the measured coherence bandwidth values are in the 150–250 MHz range. It can be seen that for two of the measurement routes the mean coherence bandwidth increases with frequency.

Fig. 25 plots the mean value of the coherence bandwidth as a function of frequency in the UMa NLOS environment.[11] It can be seen that the coherence bandwidth values are neither increasing nor decreasing with frequency. The coherence bandwidth values are observed to be < 10 MHz. This is again consistent with our earlier observations that the delay spreads do not change significantly with frequency.

Figs. 26 and 27 plot the coherence bandwidth variation with frequency for different BS heights in the UMi LOS and NLOS environments respectively. The measured coherence bandwidth values are in the 150–200 MHz range in the LOS environment and in the 5–50 MHz range in the NLOS environment. In the LOS environment, we plot the mean and standard deviation values. It can be seen that coherence bandwidth values are neither increasing nor decreasing with frequency. It is interesting to note that the coherence bandwidth values increases as the BS height increased, even though the RMS

is because of the LOS component gets more isolated and dominant as the BS height increases.

Relevant literature on Delay spread and K-factor: We now compare the delay spread and K-factor variation with frequency with the observations made in Ref. [32]. The reference summarizes the channel parameter variation with frequency from different channel measurement campaigns. For the urban street canyon LOS measurements, it was observed that the delay spreads decreased as the frequency increased from 15 GHz to 28 GHz and to 60 GHz. Also, it was stated that the K-factor increased with frequency. These findings are consistent with our observations in LOS environments. For the NLOS street canyon measurements done at frequencies 2 GHz, 15 GHz and 60 GHz, it was reported that RMS delay spreads were 150 ns and they did not change with frequency. This is again consistent with our NLOS delay spread results. These NLOS observations contradict the 3GPP model, which models decreasing RMS delay spreads with increasing frequency.

---

[11]For the NLOS scenario, the data quantization errors are quite significant. The coherence bandwidth is an integral multiple of the subcarrier spacing (0.5 MHz) and from the measured coherence bandwidth values, the ratio is less than 20. For this reason, we only plot the mean values.
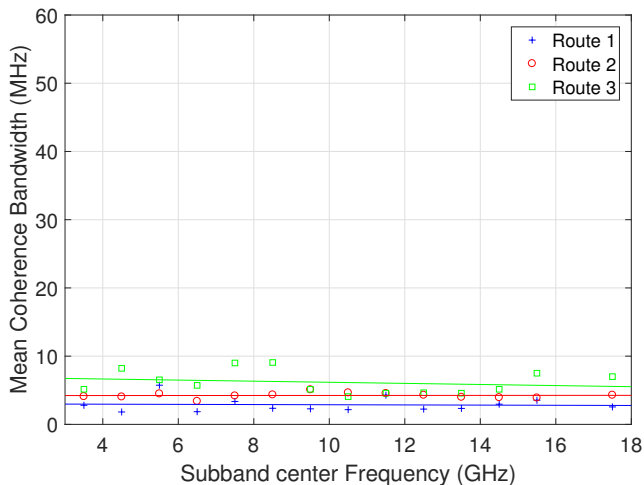
Fig. 25: Mean value of the Coherence bandwidth (MHz) for different subbands in the UMa NLOS environments. The 95% confidence intervals for the slope: $[-0.08, 0.60]$, $[0.12, 0.71]$, and $[-0.48, 0.12]$, for route 1, 2, and 3, respectively.
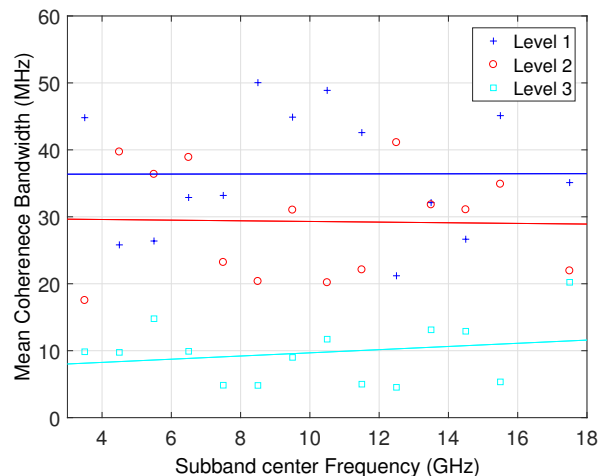

Fig. 27: Mean value of the Coherence bandwidth (MHz) for different subbands in the UMi NLOS environment. The 95% confidence intervals for the slope: $[-0.18, 0.77]$, $[-2.21, 0.15]$, and $[-0.90, 0.83]$ for the BS on level 1, 2, and 3 respectively.
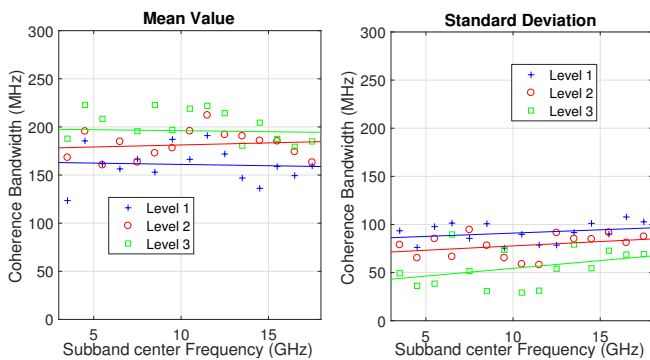

Fig. 26: Mean and standard deviation of the Coherence bandwidth (MHz) for different subbands in the UMi LOS environment. The 95% confidence intervals for the slope (mean value plot): $[-3.70, 0.80]$, $[-1.16, 2.02]$, and $[-3.25, 2.83]$ for the BS on level 1, 2, and 3 respectively.

delay spreads does not show a significant dependency in the UMi LOS environments. In the NLOS environment, we plot the mean values. The coherence bandwidth decreases with increasing BS height and these values are much higher than the ones observed in the UMa NLOS environment, where the BS height is even larger. This is consistent with our earlier observations that the subband RMS delay spreads increase with the BS height.

VI. CONCLUSIONS

We presented wireless propagation channel measurement results in the 3-18 GHz band, conducted in urban macro and micro-cellular environments. The wideband measurements were taken using a frequency-hopped multi-band channel sounder. We characterized the wideband pathloss, shadow fading and RMS delay spreads in different measurement routes for UMa LOS/NLOS environments. It has been observed that

the propagation characteristics can be significantly different in different routes–pathloss exponents varied from 1.8 to 2 in LOS environments and from 2.71 to 4.34 in NLOS environments; RMS delay spread was observed to be log normally distributed on all routes, but the parameters of the distribution were considerably different on different routes. We investigated the dependency of the channel parameters on the BS height in the UMi LOS/NLOS environments. The pathloss exponents and the RMS delay spreads increased with the BS height in NLOS environments; not significant dependency was observed in the LOS environments.

Using 1 GHz subband evaluations, we characterized the dependency of the pathloss exponents, shadow fading, RMS delay spreads, Ricean factor and coherence bandwidth on the frequency in the 3–18 GHz band. It has been observed that the RMS delay spreads roughly decrease with frequency in the LOS environments, but the delay spreads did not change significantly with frequency in the NLOS environments; the Ricean K-factor increased with frequency; the shadow fading standard deviation increased with frequency in both LOS and NLOS environments; the coherence bandwidth values did not change significantly with frequency both in LOS and NLOS environments; the pathloss exponents varied significantly with frequency, but there was no conclusive pattern in the variation. In the NLOS environment, the shadow fading was observed to be correlated between adjacent subbands and more so at the higher ends of the 3–18 GHz band.

As is the case with many channel measurement campaigns, the results presented in the paper are specific to the considered environments (TX-RX separation distances, TX/RX heights, measurement routes etc.), and more such measurements are needed to generalize the conclusions.

REFERENCES

[1] V. Kristem, C. U. Bas, R. Wang, and A. F. Molisch, "Outdoor Macro-Cellular Channel Measurements and Modeling in the 3-18 GHz Band," in *2017 IEEE Globecom Workshops (GC Wkshps)*, pp. 1–7, Dec 2017.

[2] "UMTS Forum Mobile Traffic Forecasts: 2010-2020 Report, vol. 44, umts forum, 2011," tech. rep.

[3] Y. Wang, J. Li, L. Huang, Y. Jing, A. Georgakopoulos, and P. Demestichas, "5G mobile: Spectrum broadening to higher-frequency bands to support high data rates," *IEEE Vehicular technology magazine*, vol. 9, no. 3, pp. 39–46, 2014.

[4] M. Shariat, D. M. G. Estévez, A. Vijay, K. Safjan, P. Rugeland, I. da Silva, J. Lorca, J. Widmer, M. Fresia, Y. Li, and I. Siaud, "5G Radio Access above 6 GHz," *CoRR*, vol. abs/1706.01780, 2017.

[5] A. F. Molisch, *Wireless Communications. 2nd Ed.* Hoboken, NJ, USA: Wiley-IEEE Press, 2011.

[6] L. Liu, C. Oestges, J. Poutanen, K. Haneda, P. Vainikainen, F. Quitin, F. Tufvesson, and P. D. Doncker, "The COST 2100 MIMO channel model," *IEEE Wireless Communications*, vol. 19, pp. 92–99, December 2012.

[7] M. Peter, R. Weiler, B. Göktepe, W. Keusgen, and K. Sakaguchi, "Channel Measurement and Modeling for 5G Urban Microcellular Scenarios," *Sensors*, vol. 16, no. 12, p. 1330, 2016.

[8] M. Peter, R. J. Weiler, F. Undi, F. El-Kanawati, S. Jaeckel, L. Raschkowski, L. Thiele, K. Sakaguchi, and W. Keusgen, "Investigations on the frequency dependence of the delay spread in an UMi street canyon scenario," in *2016 International Symposium on Antennas and Propagation (ISAP)*, pp. 616–617, Oct 2016.

[9] J. I. Takada, M. Kim, and K. Saito, "Characterization of Radio Propagation Channel at 11 GHz," in *European Wireless 2016; 22th European Wireless Conference*, pp. 1–6, May 2016.

[10] R. Müller, S. Häfner, D. Dupleich, R. S. Thomä, G. Steinböck, J. Luo, E. Schulz, X. Lu, and G. Wang, "Simultaneous multi-band channel sounding at mm-Wave frequencies," in *2016 10th European Conference on Antennas and Propagation (EuCAP)*, pp. 1–5, April 2016.

[11] W. Fan, I. Carton, and G. F. Pedersen, "Comparative study of centimetric and millimetric propagation channels in indoor environments," in *2016 10th European Conference on Antennas and Propagation (EuCAP)*, pp. 1–5, April 2016.

[12] W. Fan, I. Llorente, J. Nielsen, K. Olesen, and G. Pedersen, "Measured wideband characteristics of indoor channels at centimetric and millimetric bands," *EURASIP Journal on Wireless Communications and Networking*, vol. 2016, no. 58, 2016.

[13] S. Sun, T. S. Rappaport, S. Rangan, T. A. Thomas, A. Ghosh, I. Z. Kovacs, I. Rodriguez, O. Koymen, A. Partyka, and J. Jarvelainen, "Propagation Path Loss Models for 5G Urban Micro- and Macro-Cellular Scenarios," in *2016 IEEE 83rd Vehicular Technology Conference (VTC Spring)*, pp. 1–6, May 2016.

[14] A. M. Al-Samman, T. A. Rahman, M. H. Azmi, M. N. Hindia, I. Khan, and E. Hanafi, "Statistical Modelling and Characterization of Experimental mm-Wave Indoor Channels for Future 5G Wireless Communication Networks.," *PLoS ONE.*, vol. 11(9), 2016.

[15] D. Lu and D. Rutledge, "Investigation of indoor radio channels from 2.4 GHz to 24 GHz," in *IEEE Antennas and Propagation Society International Symposium. Digest. Held in conjunction with: USNC/CNC/URSI North American Radio Sci. Meeting (Cat. No.03CH37450)*, vol. 2, pp. 134–137 vol.2, June 2003.

[16] R. Naderpour, J. Vehmas, S. Nguyen, J. Järveläinen, and K. Haneda, "Spatio-temporal channel sounding in a street canyon at 15, 28 and 60 GHz," in *2016 IEEE 27th Annual International Symposium on Personal, Indoor, and Mobile Radio Communications (PIMRC)*, pp. 1–6, Sept 2016.

[17] S. Sun, T. S. Rappaport, T. A. Thomas, A. Ghosh, H. C. Nguyen, I. Z. Kovács, I. Rodriguez, O. Koymen, and A. Partyka, "Investigation of Prediction Accuracy, Sensitivity, and Parameter Stability of Large-Scale Propagation Path Loss Models for 5G Wireless Communications," *IEEE Transactions on Vehicular Technology*, vol. 65, pp. 2843–2860, May 2016.

[18] S. L. Nguyen, J. Medbo, M. Peter, A. Karttunen, K. Haneda, A. Bamba, R. D'Errico, N. Iqbal, C. Diakhate, and J.-M. Conrat, "On the Frequency Dependency of Radio Channel's Delay Spread: Analyses and Findings From mmMAGIC Multi-frequency Channel Sounding," *arXiv preprint arXiv:1712.09435*, 2017.

[19] J. Medbo, D. Sundman, H. Asplund, N. Jaldn, and S. Dwivedi, "Wireless urban propagation measurements at 2.44, 5.8, 14.8 & 58.68 GHz," in *2017 XXXIInd General Assembly and Scientific Symposium of the International Union of Radio Science (URSI GASS)*, pp. 1–4, Aug 2017.

[20] M. Sasaki, W. Yamada, T. Sugiyama, M. Mizoguchi, and T. Imai, "Path loss characteristics at 800 MHz to 37 GHz in urban street microcell environment," in *2015 9th European Conference on Antennas and Propagation (EuCAP)*, pp. 1–4, May 2015.

[21] K. Haneda, M. Peter, J. Medbo, M. Beach, R. d'Errico, S. Wu, and J. M. Conrat, "Radio channel sounding campaigns in EU H2020 mmMAGIC project for 5G channel modeling," in *2016 International Symposium on Antennas and Propagation (ISAP)*, pp. 596–597, Oct 2016.

[22] S. Jaeckel, M. Peter, K. Sakaguchi, W. Keusgen, and J. Medbo, "5G Channel Models in mm-Wave Frequency Bands," in *European Wireless 2016; 22th European Wireless Conference*, pp. 1–6, May 2016.

[23] "6–100 GHz Channel Modelling for 5G: Measurement and Modelling Plans in mmMAGIC," Feb 2016.

[24] C. U. Bas, V. Kristem, R. Wang, and A. F. Molisch, "Real-time Ultra-Wideband Frequency Sweeping Channel Sounder for 3-18 GHz," in *IEEE Military Communications Conference (MILCOM)*, pp. 775–781, 2017.

[25] V. Kristem, S. Sangodoyin, C. U. Bas, M. Käske, J. Lee, C. Schneider, G. Sommerkorn, C. J. Zhang, R. S. Thomä, and A. F. Molisch, "3D MIMO Outdoor-to-Indoor Propagation Channel Measurement," *IEEE Transactions on Wireless Communications*, vol. 16, pp. 4600–4613, July 2017.

[26] G. L. Ramos, P. Kyösti, V. Hovinen, and M. Latva-aho, "Multiple-Screen Diffraction Measurement at 10-18 GHz," *IEEE Antennas and Wireless Propagation Letters*, vol. 16, pp. 2002–2005, 2017.

[27] L. J. Greenstein, D. G. Michelson, and V. Erceg, "Moment-method estimation of the Ricean K-factor," *IEEE Communications Letters*, vol. 3, pp. 175–176, June 1999.

[28] P. Tang, J. Zhang, A. F. Molisch, P. J. Smith, M. Shafi, and L. Tian, "Estimation of the Ricean K-factor for Wideband Channel Fading," *Submitted*.

[29] A. F. Molisch, A. Karttunen, S. Hur, J. Park, and J. Zhang, "Spatially consistent pathloss modeling for millimeter-wave channels in urban environments," in *2016 10th European Conference on Antennas and Propagation (EuCAP)*, pp. 1–5, April 2016.

[30] "3GPP TSG-RAN TR 38.900, Study on channel model for frequency spectrum above 6 GHz (release 14),"

[31] I. Rodriguez, "An empirical study on radio propagation in heterogeneous networks: with focus on mobile broadband networks and small cell deployment," *PhD Thesis*, Aalborg University, 2016.

[32] M. Peter and et al., "Measurement results and final mmMAGIC channel models," *Deliverable D2.2*, May 2017, https://bscw.5g-mmmagic.eu/pub/bscw.cgi/d202656/mmMAGIC_D2-2.pdf.

[33] B. H. Fleury, "An uncertainty relation for WSS processes and its application to WSSUS systems," *IEEE Transactions on Communications*, vol. 44, pp. 1632–1634, Dec 1996.

Vinod Kristem received his Bachelor of Technology from the National Institute of Technology (NIT), Warangal in 2007; Master of Engineering degree in Telecommunications from the Indian Institute of Science, Bangalore, India in 2009; Ph.D. degree in Electrical Engineering from University of Southern California, Los Angeles in 2017. From 2009 to 2011, he was with Broadcom Corp. He is currently a Research Scientist at Intel Corporation working on next generation WiFi. His research interests include multi-antenna systems, Ultrawideband systems, channel measurements and modeling.

C. Umit Bas received the B.Sc. and M.Sc. degrees in electrical and electronics engineering from Koc University, Turkey, in 2010 and 2012, respectively. He is currently pursuing the Ph.D. degree advised by Dr. Andreas F. Molisch in the Department of Electrical Engineering, University of Southern California, USA. He is also serving as the co-manager of the UltraLab. His research interests include design and construction of real-time channel sounders for millimeter-wave and ultra-wideband communications, and wireless propagation channel measurements and modeling.

Rui Wang received the B.S. degree from Southeast University, Nanjing, China in 2010 and the M.S. degree (Hons.) in 2012 from the University of Southern California, Los Angeles, CA, USA. He is currently a Ph.D. Candidate with the WiDeS Group at Ming-Hsieh Department of Electrical Engineering, University of Southern California. His research interests include wireless channel measurements and modeling for vehicle-to-vehicle and mm-wave communication systems. He is also interested in statistical signal processing and optimization algorithms.

Andreas F. Molisch received the Dipl. Ing., Ph.D., and habilitation degrees from the Technical University of Vienna, Vienna, Austria, in 1990, 1994, and 1999, respectively. He subsequently was with AT&T (Bell) Laboratories Research (USA); Lund University, Lund, Sweden, and Mitsubishi Electric Research Labs (USA). He is now a Professor and Solomon-Golomb–Andrew-and-Erna-Viterbi Chair at the University of Southern California, Los Angeles.

His current research interests are the measurement and modeling of mobile radio channels, multi-antenna systems, ultra-wideband communications and localization, novel modulation and multiple access systems, and wireless video distribution. He has authored, coauthored, or edited four books (among them the textbook Wireless Communications, Wiley-IEEE Press), 19 book chapters, more than 220 journal papers, 300 conference papers, as well as more than 80 patents and 70 standards contributions.

Dr. Molisch has been an Editor of a number of journals and special issues, General Chair, Technical Program Committee Chair, or Symposium Chair of multiple international conferences, as well as Chairman of various international standardization groups. He is a Fellow of the National Academy of Inventors, Fellow of the AAAS, Fellow of the IEEE, Fellow of the IET, an IEEE Distinguished Lecturer, and a member of the Austrian Academy of Sciences. He has received numerous awards, among them the Donald Fink Prize of the IEEE, the IET Achievement Medal, and the Eric Sumner Award of the IEEE.